

ious spectroscopic measurements^{6–9}, but a direct quantitative comparison requires knowledge of various physical parameters involved in a specific experiment.

A direct quantitative comparison between theory and measurement is possible, however, for the specific heat. The measured specific heat^{3–5} of MgB₂ at low temperature is substantial, and a large hump appears at about 10 K that is inconsistent with a one-gap BCS model. We have calculated the specific heat from the free energy of the superconducting state. The overall shape and magnitude of our calculated specific-heat curve agrees very well with the experimental data, especially below 30 K (Fig. 4). We find that the low-temperature hump in our calculated curve and in the experimental data is caused by the existence of low-energy excitations across the small superconducting energy gap of the π -bonding states. □

Received 14 November 2001; accepted 31 May 2002; doi:10.1038/nature00898.

1. Nagamatsu, J., Nakagawa, N., Muranaka, T., Zenitani, Y. & Akimitsu, J. Superconductivity at 39 K in magnesium diboride. *Nature* **410**, 63–64 (2001).
2. Hinks, D. G., Claus, H. & Jorgensen, J. D. The complex nature of superconductivity in MgB₂ as revealed by the reduced total isotope effect. *Nature* **411**, 457–460 (2001).
3. Wang, Y., Plackowski, T. & Junod, A. Specific heat in the superconducting and normal state (2–300 K, 0–16 T), and magnetic susceptibility of the 38 K superconductor MgB₂. *Physica C* **355**, 179–193 (2001).
4. Bouquet, F., Fisher, R. A., Phillips, N. E., Hinks, D. G. & Jorgensen, J. D. Specific heat of Mg¹¹B₂: evidence for a second energy gap. *Phys. Rev. Lett.* **87**, 047001–1–047001–4 (2001).
5. Yang, H. D. et al. Order parameter of MgB₂: a fully gapped superconductor. *Phys. Rev. Lett.* **87**, 167003–1–167003–4 (2001).
6. Szabo, P. et al. Evidence for two superconducting energy gaps in MgB₂ by point-contact spectroscopy. *Phys. Rev. Lett.* **87**, 137005–1–137005–4 (2001).
7. Giubileo, F. et al. Two-gap state density in MgB₂: a true bulk property or a proximity effect? *Phys. Rev. Lett.* **87**, 177008–1–177008–4 (2001).
8. Chen, X. K., Konstantinovi, M. J., Irwin, J. C., Lawrie, D. D. & Franck, J. P. Evidence for two superconducting gaps in MgB₂. *Phys. Rev. Lett.* **87**, 157002–1–157002–4 (2001).
9. Tsuda, S. et al. Evidence for a multiple superconducting gap in MgB₂ from high-resolution photoemission spectroscopy. *Phys. Rev. Lett.* **87**, 177006–1–177006–4 (2001).
10. Kortus, J., Mazin, I. I., Belashchenko, K. D., Antropov, V. P. & Boyer, L. L. Superconductivity of metallic boron in MgB₂. *Phys. Rev. Lett.* **86**, 4656–4659 (2001).
11. An, J. M. & Pickett, W. E. Superconductivity of MgB₂: covalent bonds driven metallic. *Phys. Rev. Lett.* **86**, 4366–4369 (2001).
12. Bohnen, K.-P., Heid, R. & Renker, B. Phonon dispersion and electron-phonon coupling in MgB₂ and AlB₂. *Phys. Rev. Lett.* **86**, 5771–5774 (2001).
13. Yildirim, T. et al. Giant anharmonicity and nonlinear electron-phonon coupling in MgB₂: a combined first-principles calculation and neutron scattering study. *Phys. Rev. Lett.* **87**, 037001–1–037001–4 (2001).
14. Liu, A. Y., Mazin, I. I. & Kortus, J. Beyond Eliashberg superconductivity in MgB₂: anharmonicity, two-phonon scattering, and multiple gaps. *Phys. Rev. Lett.* **87**, 087005–1–087005–4 (2001).
15. Kong, Y., Dolgov, O. V., Jepsen, O. & Andersen, O. K. Electron-phonon interaction in the normal and superconducting states of MgB₂. *Phys. Rev. B* **64**, 020501–1–020501–4 (2001).
16. Choi, H. J., Roundy, D., Sun, H., Cohen, M. L. & Louie, S. G. First-principles calculation of the superconducting transition in MgB₂ within the anisotropic Eliashberg formalism. *Phys. Rev. B* **66**, 020513–1–020513–4 (2002).
17. Eliashberg, G. M. Interactions between electrons and lattice vibrations in a superconductor. *Zh. Eksp. Teor. Fiz.* **38**, 966–976 (1960); *Sov. Phys. JETP* **11**, 696–702 (1960).
18. Allen, P. B. & Mitrović, B. In *Solid State Physics* (eds Ehrenreich, H., Seitz, F. & Turnbull, D.) Vol. 37 1–92 (Academic, New York, 1982).
19. Carbotte, J. P. Properties of boson-exchange superconductors. *Rev. Mod. Phys.* **62**, 1027–1157 (1990).
20. Marsiglio, F., Schossmann, M. & Carbotte, J. P. Iterative analytic continuation of the electron self-energy to the real axis. *Phys. Rev. B* **37**, 4965–4969 (1988).
21. Karapetrov, G., Iavarone, M., Kwok, W. K., Crabtree, G. W. & Hinks, D. G. Scanning tunneling spectroscopy in MgB₂. *Phys. Rev. Lett.* **86**, 4374–4377 (2001).
22. Sharoni, A., Felner, I. & Millo, O. Tunneling spectroscopy and magnetization measurements of the superconducting properties of MgB₂. *Phys. Rev. B* **63**, 220508–1–220508–4 (2001).
23. Rubio-Bollinger, G., Suderow, H. & Vieira, S. Tunneling spectroscopy in small grains of superconducting MgB₂. *Phys. Rev. Lett.* **86**, 5582–5584 (2001).
24. Schmidt, H., Zasadzinski, J. F., Gray, K. E. & Hinks, D. G. Energy gap from tunneling and metallic contacts onto MgB₂: possible evidence for a weakened surface layer. *Phys. Rev. B* **63**, 220504–1–220504–4 (2001).
25. Takahashi, T., Sato, T., Souma, S., Muranaka, T. & Akimitsu, J. High-resolution photoemission study of MgB₂. *Phys. Rev. Lett.* **86**, 4915–4917 (2001).
26. Buzea, C. & Yamashita, T. Review of superconducting properties of MgB₂. *Supercond. Sci. Technol.* **14**, R115–R146 (2001).
27. Suhl, H., Matthias, B. T. & Walker, L. R. Bardeen-Cooper-Schrieffer theory of superconductivity in the case of overlapping bands. *Phys. Rev. Lett.* **3**, 552–554 (1959).
28. Bardeen, J. & Stephen, M. Free-energy difference between normal and superconducting states. *Phys. Rev. A* **136**, 1485–1487 (1964).

Acknowledgements

This work was supported by the National Science Foundation and by the Director, Office of Science, Office of Basic Energy Sciences of the US Department of Energy.

Computational resources have been provided by the National Science Foundation at the National Center for Supercomputing Applications and by the National Energy Research Scientific Computing Center. H. S. acknowledges financial support from the Berkeley Scholar Program funded by the Tang Family Foundation.

Competing interests statement

The authors declare that they have no competing financial interests.

Correspondence and requests for materials should be addressed to S.G.L. (e-mail: sglouie@uclink.berkeley.edu).

The influence of a chemical boundary layer on the fixity, spacing and lifetime of mantle plumes

A. Mark Jellinek & Michael Manga

Department of Earth and Planetary Science, University of California, Berkeley, California 94720, USA

Seismological observations provide evidence that the lowermost mantle contains superposed thermal and compositional boundary layers¹ that are laterally heterogeneous^{2,3}. Whereas the thermal boundary layer forms as a consequence of the heat flux from the Earth’s outer core, the origin of an (intrinsically dense) chemical boundary layer remains uncertain⁴. Observed zones of ‘ultra-low’ seismic velocity⁵ suggest that this dense layer may contain metals^{6,7} or partial melt⁸, and thus it is reasonable to expect the dense layer to have a relatively low viscosity. Also, it is thought that instabilities in the thermal boundary layer could lead to the intermittent formation and rise of mantle plumes. Flow into ascending plumes can deform the dense layer, leading, in turn, to its gradual entrainment^{9–14}. Here we use analogue experiments to show that the presence of a dense layer at the bottom of the mantle induces lateral variations in temperature and viscosity that, in turn, determine the location and dynamics of mantle plumes. A dense layer causes mantle plumes to become spatially fixed, and the entrainment of low-viscosity fluid enables plumes to persist within the Earth for hundreds of millions of years.

Convective motions driven by core cooling have a structure that is three-dimensional and time-dependent. Consequently, the dynamics of the interaction between this flow and an underlying dense layer is complex. Because of the computational challenge of resolving small (kilometre) length scales while tracking viscosity and density interfaces¹⁵, numerical simulations for conditions appropriate to mantle convection are typically limited to two dimensions^{12,13}, though three-dimensional simulations are currently being performed¹⁴. Laboratory experiments are thus often used to study thermochemical convection, and the experiments presented here extend previous investigations^{9,10,16} to the situation in which the dense layer is thin and has a low viscosity. Here we need to distinguish ‘plumes’ from ‘thermals’: we use ‘plume’ to describe buoyant upwellings (or downwellings) that extend continuously from the hot (or cold) boundary layer, and ‘thermal’ to indicate a discrete buoyant blob. Under conditions of thermal equilibrium, more-viscous cold fluid descends in narrow sheet-like plumes¹⁷, whereas lower-viscosity hot fluid ascends mostly in thermals^{18,19}.

Our experiments are performed in the tank illustrated in Fig. 1 (the legend of Fig. 1 also defines the parameters and variables). An initial series of 23 experiments without a dense layer is performed to provide a framework to interpret the more complicated situation

including a dense layer. Both free-slip and no-slip bottom boundaries are used. The tank is filled with a single layer of polybutene oil (Chevron Oronite 16500), which is a very viscous, colourless newtonian fluid. Before the start of each experiment the oil layer is heated from below and cooled from above until thermal equilibrium is achieved. Time-lapse video, and measurements of the surface heat flux, surface temperature and interior temperature as a function of time are used to characterize flows quantitatively. Thermal equilibrium is indicated by constant and equal heat fluxes at the roof and floor of the tank, and by an interior fluid temperature that is statistically constant over time. Experiments are run for several days, corresponding to thousands of plume rise times. Here, a ‘rise time’ is defined as the timescale for a thermal or plume to ascend from the hot thermal boundary layer to the roof of the tank.

The second series of experiments is designed specifically to understand the interaction between convection driven by heat flow from the core and an underlying dense, low-viscosity layer under conditions appropriate to the Earth’s mantle. We first allow the convecting fluid to reach thermal equilibrium, and then introduce dense, low-viscosity, miscible soybean oil through a 4-mm-diameter port in a corner of the tank (Fig. 2). This dense fluid (coloured red) spreads over the floor of the tank, driving no apparent large-scale circulation, and forms a nearly isothermal layer that is 0.5 cm high. Following its introduction, this ‘dense layer’ is deformed by flow of thermal boundary layer fluid into ascending thermals of polybutene oil (the ‘ambient fluid’). Figure 2 shows circular embayments separated by sharp ‘divides’ that formed early in the evolution of the red, dense layer. The dynamic coupling between topography and motions driven by lateral temperature variations stabilize the pattern of flow over timescales much longer than a plume rise time; buoyant fluid is able to ascend along the sloping interface with the low-viscosity soybean oil more easily than rise vertically into the more-viscous ambient fluid. To confirm this mechanism and to understand the influences of topography on the dense layer and the viscosity ratio λ_d , we performed 18 additional experiments. Figure 3 shows that smaller (but still finite) topographic relief is needed to stabilize the positions of plumes when λ_d

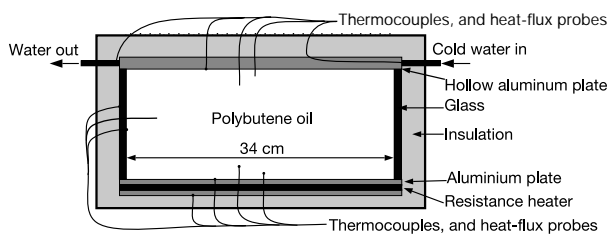


Figure 1 A schematic illustration of the apparatus used for the experiments shown in Figs 2 and 4 (ref. 26). The interior of the tank has a depth of 17 cm. Five dimensionless parameters are used to characterize our experiments and scale the results to the Earth’s mantle. (1) The Rayleigh number, $Ra = \rho g \alpha \Delta T H^3 / \mu_c \kappa > 10^5$; (2) the Prandtl number, $Pr = \mu_c / \rho \kappa > 10^4$. Consequently, flows are laminar (low Reynolds number), time-dependent and composed predominantly of blobs ascending (or descending) from the hot (or cold) boundaries²⁷. Here, H is the combined height of both fluid layers, g the acceleration due to gravity, ΔT the temperature difference across the height H , ρ the fluid density, α the coefficient of thermal expansion, κ the thermal diffusivity, and μ_c , μ_h and μ_d are the viscosities evaluated in the ambient fluid, at the interface with the hot boundary and in the dense layer, respectively. (3) The ratio of the buoyancies of the dense layer to the thermal boundary layer, $B = \Delta \rho / \rho \alpha \Delta T$, where $\Delta \rho$ is the intrinsic density difference between the dense layer and overlying fluid, indicates the gravitational stability of the dense layer. $B < 1$ can still be stable because ΔT is based on the full temperature difference across the convecting system rather than the smaller temperature difference across the hot thermal boundary layer¹⁶. We choose this definition because ΔT is an externally controlled variable. (4) The viscosity ratio $\lambda_d = \mu_c / \mu_d$, and (5) the viscosity ratio $\lambda_h = \mu_c / \mu_h$; both of these ratios depend on temperature.

is large. The spacing between the centres of the embayments remains approximately constant, apparently governed by the wavelength of the first Rayleigh–Taylor instability of the thermal boundary layer (discussed in more detail later). Stable flows are enhanced because entrainment of the dense layer establishes narrow, cylindrical low-viscosity conduits beneath ascending thermals (Fig. 4), causing a transition from an unsteady flow dominated by upwelling thermals to a steady flow governed by axisymmetric plumes with persistent trailing conduits. Finite deformation of the dense layer is needed to stabilize plume locations, because a flat boundary permits only thermals to form (Fig. 4b).

Our results suggest that the persistence, fixity and composition of mantle plumes can depend on the mechanics of entrainment from, and the longevity of, a dense layer. Accordingly, we extend previous studies^{9,11,16,20,21} by developing scaling relationships for the radius of entrained low-viscosity tendrils and the erosion rate of the dense layer. We first consider entrainment by flow into thermals forming at the hot boundary. Second, we address entrainment by flow into established conduits.

Flow into an ascending thermal or an established plume conduit drags a layer of material from the dense layer. Assuming $\Delta \rho > 0$, $\lambda_d \gg 1$ and that the entrained tendril of fluid is thin relative to the thickness of the thermal boundary layer, a balance of viscous (drag)

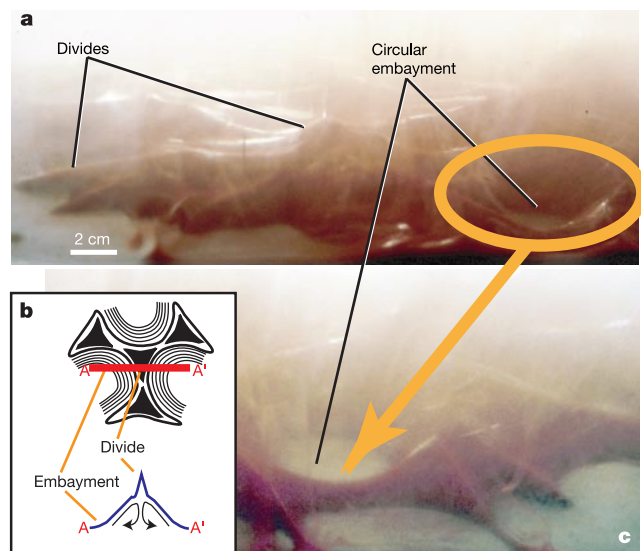


Figure 2 Photographs showing an oblique view of the temporal evolution of a dense, low-viscosity layer of soybean oil (coloured red) emplaced at the base of a vigorously convecting layer of polybutene oil (colourless). Here, $Ra = 3.6 \times 10^7$, $B = 0.56$, $\lambda_d = 1.1 \times 10^2$ and $\lambda_h = 2.7$. The ratio of the height of the dense layer D (0.5 cm) to the total height of the system H (17 cm) is chosen to be an analogue for the ratio of the height of dense layer (a few hundred kilometres, say) to the height of the mantle (3,000 km). Initially, the spreading of dense soybean oil imparts a thermal transient to the bottom boundary. However, because the height of the dense layer is comparable to the thickness of the thermal boundary layer, thermal equilibrium is reacquired over the timescale for emplacement of the layer. **a**, Subsequent entrainment from the dense layer by flow into ascending thermals produces circular embayments and divides that, in turn, determine the style of convection from the hot boundary. Dynamically, horizontal temperature gradients drive flow from the tank floor, up the sides of embayments to peaks on the divides, where upwellings into the ambient fluid become fixed (compare Fig. 3). **b**, A schematic contour map and cross-section illustrating the topography in **a**. Arrows indicate motions within the dense layer, and show the nature of the predominantly mechanical coupling (but also thermal coupling—see Fig. 4) between the two layers. **c**, Approximately 120 plume rise times later in the experiment (equivalent to 3.6 Gyr of Earth’s history), upwellings remain controlled by the positions of divides and embayments formed at the start of the experiment (although embayments have been eroded significantly).

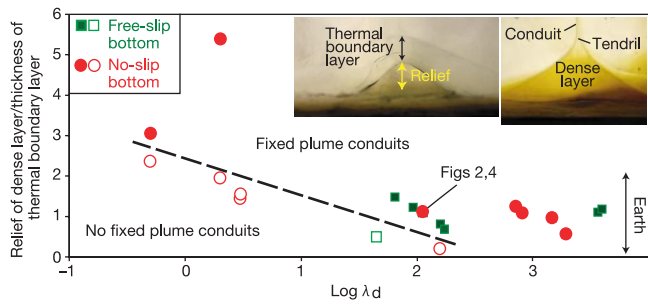


Figure 3 Plot summarizing the conditions leading either to spatially fixed (filled symbols) or not-fixed (open symbols) plumes. Except where indicated, the data are obtained using the method and apparatus of ref. 16. Circles, from experiments with a no-slip bottom boundary condition; squares, from experiments in which a free-slip lower boundary is obtained using the method of ref. 28. When λ_d is large ($>10^2$), buoyant fluid ascends along the sloping interface with the dense layer (rather than vertically)²⁹ because the underlying low-viscosity soybean oil presents a smaller retarding drag force than the more-viscous ambient fluid. When λ_d is small (~ 1), the viscous stresses due to the dense layer and interior fluid are similar. So for $\lambda_d < 10$, the relief must be comparable to, or greater than, the thickness of the thermal boundary layer to cause the convection to be governed by steady flow into long-lived, stationary plume conduits. Smaller topographic relief results in unsteady flow, in which plumes have a spacing and lifetime that is approximately stochastic. As λ_d becomes very large, however, increasingly less (but still finite; Fig. 4) relief is required to cause the convection to become governed by fixed plumes. The dashed line schematically separates conditions leading to fixed or not-fixed plumes. This line cannot be extrapolated to the horizontal axis because topographic relief on the dense layer is required for fixed plumes.

and buoyancy forces¹¹ leads to a scale for the radius of an entrained tendrils:

$$l \approx \left(\frac{\mu_d V}{g \Delta \rho} \right)^{1/2} = \left(\frac{H^3 V}{\kappa B R a \lambda_d} \right)^{1/2} \quad (1)$$

For thermals, an appropriate velocity, V , is the rise speed $V_{th} \approx \kappa H^{-1} Ra^{1/3}$ (ref. 22) and equation (1) thus becomes:

$$l_{th} \approx \left(\frac{H^2}{\lambda_d B R a^{2/3}} \right)^{1/2} \quad (2)$$

An estimate of the average erosion rate of the dense layer by flow into rising thermals (or conduits) depends on the area of the region of thermal-boundary-layer fluid feeding each type of upwelling. Hence, we require constraints on the horizontal spacing between upwellings. The measured average horizontal spacing between 6–8 established conduits in the experiment shown in Figs 2 and 4 is approximately constant, and between 8 and 10 cm. For a critically unstable thermal boundary layer of thickness $10 H R a^{-1/3}$ (ref. 22) embedded between an underlying low-viscosity dense layer and overlying more-viscous ambient fluid, linear stability theory²³ constrains the most unstable wavelength:

$$L \approx \frac{20 \pi H}{C} \left(\frac{\lambda_h}{R a} \right)^{1/3} \quad (3)$$

where the constant $C \approx 0.6$ depends on λ_h , λ_d and B ; here, L is ≈ 7.8 cm. The consistency between measurements and theory suggests that the spacing between plumes is governed by the first Rayleigh–Taylor instability of the buoyant thermal boundary layer following the introduction of the dense layer. The fact that conduit spacing can be predicted with linear theory is important for two reasons. First, this finding supports our argument that the dynamic coupling between rising thermals and an underlying dense layer leads to upwellings that remain fixed spatially. Second, a scale for the horizontal spacing between upwellings may now be written explicitly in terms of parameters controlled externally. Consequently, the

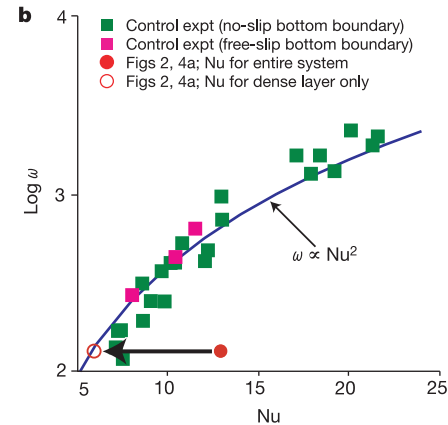
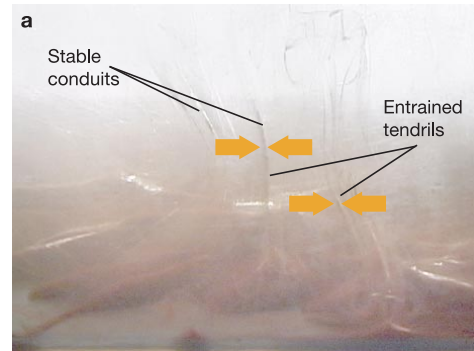


Figure 4 Illustration of the spatial and temporal structure of plumes. **a**, Photograph illustrating persistent, axisymmetric, low-viscosity conduits behind rising thermals. Once formed, conduits govern the flow of buoyant fluid from the hot boundary and persist until the dense layer is eroded completely. Hence, the conduits are regarded as stable structures. The arrows indicate entrained tendrils of dense fluid. Tendril radii, which are measured near the bases of 6–8 established conduits during an experiment, are in the range 0.25–1 mm with a mean of 0.6 mm, and constrain the scaling constant, $\Delta = 0.7$. The average vertical flux per area of dense fluid, which is obtained from time-lapse video, is about 3–5 mm h⁻¹. **b**, The frequency of thermal formation, ω , made dimensionless with the conductive timescale, H^2/κ , as a function of Nusselt number, Nu (the measured dimensionless heat flux). ω is obtained with heat-flux probes, thermocouples and visually. Solid squares are control experiments performed without a dense layer with no-slip and free-slip lower boundaries. The theoretical curve ($\omega \propto Nu^2$) is in agreement with the control experiments and is compatible with convection from the hot boundary being in the form of intermittent thermals¹⁹. The data shown are from the dense-layer experiment shown in **a** and in Fig. 2. Filled and open circles are based on Nu for the entire system and for the dense layer, respectively. At the start of the experiment (Fig. 2a) ω is reduced by about a factor of 5, compared with a flow transporting the same amount of heat without a dense layer. The measured frequency implies that thermals in the ambient fluid are coupled to the flow in the dense layer. Once conduits become established, however, no characteristic frequency is observed, and the flow is steady. After the erosion of the dense layer, the flow evolves back to intermittent thermals as in the control experiments.

erosion rate of dense layer by flow into rising thermals is

$$q_{th} \approx V_{th} \frac{l^2}{L^2} = \frac{C^2}{20^2 \pi^2} \left(\frac{\kappa}{H} \right) \frac{Ra^{1/3}}{\lambda_d B \lambda_h^{2/3}} \quad (4)$$

When convection is governed by established plume conduits, scaling arguments for both the tendrils radius l_{pl} and the erosion rate q_{pl} depend on the spacing between plumes^{20,21}. In this case, the flow velocity²¹ V_{pl} is given approximately by $(\kappa/H)(L/H)Ra^{2/3}$. Thus, from equations (1) and (3) the average tendrils radius is:

$$l_{pl} = 10.2 \Delta H \left(\frac{\lambda_h^{1/3}}{\lambda_d B R a^{2/3}} \right)^{1/2} \quad (5)$$

The measured l_{pl} is 0.6 mm (Fig. 4 legend), implying that the constant $\Lambda = 0.7$.

Time-lapse video is used to measure the average erosion rate of the dense layer by flow into established conduits. The time-derivative of the position of the density interface indicates an average erosion rate of 3–5 mm h⁻¹. From equations (3) and (5), the erosion rate is

$$q_{pl} = V_{pl} \frac{l_{pl}^2}{L^2} = \frac{\Lambda^2 \kappa Ra^{1/3}}{H \lambda_d B} \quad (6)$$

which is consistent with refs 9 and 16, and which predicts $q_{pl} = 5 \text{ mm h}^{-1}$ (Fig. 3).

Applying our results to the Earth requires constraints on Ra , B , λ_d and λ_h . Ra for mantle convection driven by core cooling is in the range 10^7 – 10^8 . The data in Fig. 3 imply that λ_d needs to be in excess of 10^1 – 10^2 in order for fixed plumes to occur. In addition, we take $\lambda_h = 10^2$ (ref. 24) and $B = 0.5$, along with typical values of $\kappa = 10^{-6} \text{ m}^2 \text{ s}^{-1}$ and $H = 3 \times 10^6 \text{ m}$. Assuming that mantle starting plumes are dynamically similar to thermals, equations (2) and (4) imply that tendrils entrained by flow into starting plumes are less than 1 km in radius, and that the associated erosion rates are of the order of 10^{-8} – $10^{-7} \text{ km Myr}^{-1}$. On the other hand, because $V_{pl} \gg V_{th}$, equations (5) and (6) predict that tendrils entrained into established low-viscosity conduits are 5–10 km in radius, and the resultant entrainment rate is expected to be of the order of 10^{-2} – $10^{-3} \text{ km Myr}^{-1}$. If a typical dense layer is, say, 100–300 km high, these erosion rates imply that the layer could persist for times comparable to, or longer than, the age of the Earth. Finally, equation (3) predicts that, in the presence of a dense layer, the spacing between mantle plumes is of the order of 10^3 km . This value is compatible with the distribution of hotspots in the Pacific, which appear to overlie the ultra-low-velocity zone³, when their positions are extrapolated to the core–mantle boundary^{3,25,30}.

We have shown that a dense, low-viscosity compositional boundary layer at the base of the mantle may determine the location, relative fixity and spacing of mantle plumes. Moreover, we have argued that entrainment from this low-viscosity layer may influence the composition of plumes and be important in establishing long-lived, low-viscosity conduits extending from the thermal boundary layer at the base of the mantle to the base of the lithosphere. Our results may resolve a basic conundrum in mantle dynamics—that hotspots remain approximately fixed in space relative to each other for timescales much longer than the time required for a plume to rise through the mantle. □

Received 26 October 2001; accepted 15 July 2002; doi:10.1038/nature00979.

1. Lay, T., Williams, Q. & Garnero, E. J. The core–mantle boundary layer and deep Earth dynamics. *Nature* **392**, 461–468 (1998).
2. Wyssession, M. E. Large-scale structure at the core–mantle boundary from diffracted waves. *Nature* **382**, 244–248 (1996).
3. Castle, J. C., Creager, K. C., Winchester, J. P. & van der Hilst, R. D. Shear wave speeds at the base of the mantle. *J. Geophys. Res.* **105**, 21543–21557 (2000).
4. Gurnis, M., Wyssession, M. E., Knittle, E. & Buffett, B. A. (eds) *The Core–Mantle Region Monograph 28* (American Geophysical Union, Washington DC, 1998).
5. Garnero, E. J. Heterogeneity of the lowermost mantle. *Annu. Rev. Earth Planet. Sci.* **28**, 509–537 (2000).
6. Knittle, E. & Jeanloz, R. The Earth's core–mantle boundary: Results of experiments at high pressures and temperatures. *Science* **251**, 1438–1453 (1991).
7. Brandon, A. D. *et al.* Coupled ¹⁸⁶Os and ¹⁸⁷Os evidence for core–mantle interaction. *Science* **280**, 1570–1573 (1998).
8. Williams, Q. & Garnero, E. J. Seismic evidence for partial melt at the base of the Earth's mantle. *Science* **273**, 1528–1530 (1996).
9. Davaille, A. Simultaneous generation of hotspots and superswells by convection in a heterogeneous planetary mantle. *Nature* **402**, 756–760 (1999).
10. Olson, P. & Kincaid, C. Experiments on the interaction of thermal convection and compositional layering at the base of the mantle. *J. Geophys. Res.* **96**, 4347–4354 (1991).
11. Sleep, N. H. Gradual entrainment of a chemical layer at the base of the mantle by overlying convection. *Geophys. J. Int.* **95**, 437–447 (1998).
12. Montague, N. L. & Kellogg, L. H. Numerical models of a dense layer at the base of the mantle and implications for the geodynamics of D'. *J. Geophys. Res.* **105**, 11101–11114 (2000).
13. Farnetani, C. G. Excess temperature of mantle plumes: the role of chemical stratification across D'. *Geophys. Res. Lett.* **24**, 1583–1586 (1997).

14. Tackley, P. J. The strong heterogeneity caused by deep mantle layering. *Geochem. Geophys. Geosyst.* **3**, U1–U22 (2002).
15. van Keken, P. E. *et al.* A comparison of methods for the modeling of thermochemical convection. *J. Geophys. Res.* **102**, 22477–22495 (1997).
16. Gonnermann, H. M., Manga, M. & Jellinek, A. M. Dynamics and longevity of an initially stratified mantle. *Geophys. Res. Lett.* **29**, 10.1029/2002GL014851 (2002).
17. Neavel, K. E. & Johnson, A. M. Entrainment in compositionally buoyant plumes. *Tectonophysics* **200**, 1–15 (1991).
18. Manga, M. & Weeraratne, D. Experimental study of non-Boussinesq Rayleigh–Benard convection at high Rayleigh and Prandtl numbers. *Phys. Fluids* **11**, 2969–2976 (1999).
19. Sparrow, E. M., Husar, R. B. & Goldstein, R. J. Observations and other characteristics of thermals. *J. Fluid Mech.* **41**, 793–802 (1970).
20. Davaille, A. Two-layer thermal convection in miscible viscous fluids. *J. Fluid Mech.* **379**, 223–253 (1999).
21. Olson, P., Schubert, G. & Anderson, C. Structure of axisymmetric mantle plumes. *J. Geophys. Res.* **98**, 6829–6844 (1993).
22. Turner, J. S. *Buoyancy Effects in Fluids* (Cambridge Univ. Press, Cambridge, 1973).
23. Lister, J. R. & Kerr, R. C. The effect of geometry on the gravitational instability of a buoyant region of viscous fluid. *J. Fluid Mech.* **202**, 577–594 (1989).
24. Nataf, H.-C. Mantle convection, plates, and hotspots. *Tectonophysics* **187**, 361–377 (1991).
25. Sleep, N. H. Time dependence of mantle plumes: Some simple theory. *J. Geophys. Res.* **97**, 20007–20019 (1992).
26. Schaeffer, N. & Manga, M. Interaction of rising and sinking mantle plumes. *Geophys. Res. Lett.* **28**, 455–458 (2001).
27. Neavel, K. E. & Johnson, A. M. Entrainment in compositionally buoyant plumes. *Tectonophysics* **200**, 1–15 (1991).
28. Jellinek, A. M., Lenardic, A. & Manga, M. The influence of interior mantle temperature on the structure of plumes: Heads for Venus, Tails for the Earth. *Geophys. Res. Lett.* **29**, 10.1029/2001GL014624 (2002).
29. Martin, D. & Campbell, I. H. Laboratory modeling of convection in magma chambers: Crystallization against sloping floors. *J. Geophys. Res.* **93**, 7974–7988 (1988).
30. Steinberger, B. & O'Connell, R. J. Advection of plumes in mantle flow: implications for hotspot motion, mantle viscosity and plume distribution. *Geophys. J. Int.* **132**, 412–434 (1998).

Acknowledgements

We thank A. Davaille for comments on the previous version of the manuscript, and L. H. Kellogg, R. C. Kerr, M. A. Richards and N. Sleep for comments on earlier versions. This work was supported by the National Science Foundation and The Miller Institute for Basic Research in Science.

Competing interests statement

The authors declare that they have no competing financial interests.

Correspondence and requests for materials should be addressed to A.M.J. (e-mail: markj@seismo.berkeley.edu).

.....
Seismic evidence for catastrophic slab loss beneath Kamchatka

Vadim Levin*, **Nikolai Shapiro*†**, **Jeffrey Park*** & **Michael Ritzwoller*†**

* *Department of Geology and Geophysics, Box 208109, Yale University, New Haven, Connecticut 06520, USA*

† *Department of Physics, University of Colorado, Boulder, Colorado 80309, USA*

.....
 In the northwest Pacific Ocean, a sharp corner in the boundary between the Pacific plate and the North American plate joins a subduction zone running along the southern half of the Kamchatka peninsula¹ with a region of transcurrent motion along the western Aleutian arc^{1,2}. Here we present images of the seismic structure beneath the Aleutian–Kamchatka junction and the surrounding region, indicating that: the subducting Pacific lithosphere terminates at the Aleutian–Kamchatka junction; no relic slab underlies the extinct northern Kamchatka volcanic arc; and the upper mantle beneath northern Kamchatka has unusually slow shear wavespeeds. From the tectonic and volcanic evolution of Kamchatka over the past 10 Myr (refs 3–5) we infer that at least two episodes of catastrophic slab loss have occurred. About 5 to 10 Myr ago, catastrophic slab loss shut down island-arc volcanic